2024 IEEE Conference on Control Technology and Applications (CCTA)
August 21-23, 2024. Newcastle upon Tyne, UK

Quintuple Thermal Model for All-Solid-State Batteries and Temperature Estimation through a Cascaded Thermal-Electrochemical Model

Patryck Ferreira and Shu-Xia Tang

2024 IEEE Conference on Control Technology and Applications (CCTA) | 979-8-3503-7094-2/24/$31.00 ©2024 IEEE | DOI: 10.1109/CCTA60707.2024.10666604

***Abstract*— This study introduces a novel quintuple thermal model for all-solid-state batteries, governed by five Ordinary Differential Equations (ODEs) representing the temperatures of the case surface near the cathode, cathode, electrolyte, anode, and the case surface near the anode. The thermal model estimates temperatures by utilizing heat generated from the battery, derived from an electrochemical model that describes the concentration of lithium-ions in the cathode and electrolyte through two Partial Differential Equations (PDEs). Model reduction, achieved via Padé approximation, transforms the PDEs into four 5th-order transfer functions. The thermal model is verified using ANSYS Transient Thermal Analysis. Optimal sensor placement was implemented with a single observable option using just one sensor. Subsequently, the Kalman filter was used to estimate the temperature.**

***Index Terms*— All-Solid-State Batteries, Thermal Model, Electrochemical Model, Kalman Filter, Padé Approximation.**

I. Introduction

All-Solid-State Batteries (ASSBs) offer promising advancements in energy storage due to their use of solid electrolytes. These innovative batteries eliminate the use of flammable liquid electrolytes found in conventional Lithium-ion Batteries (LiBs), significantly reducing the risk of fire and explosion [1]. Compared to lithium-ion batteries, ASSBs can store more energy within the same volume, making them a compelling choice for various applications [2]. In addition to their high energy density, ASSBs hold the capability to support ultra-fast charging, thereby considerably reducing charging times [3].

Temperature is a critical factor for the safety of ASSBs. The operating temperature also affects the ionic conductivity and diffusion of lithium-ions within the solid-state electrolyte, which can impact the performance and energy density of the battery [4]. Furthermore, high operating temperatures can also accelerate the degradation of electrode materials and solid-state electrolytes, which can result in decreased battery capacity and cycle life [5].

The contributions of this study are summarized as follows:

- This article introduces a novel thermal model for ASSBs. In contrast, models such as [6] focus on LiBs, predicting temperatures only in the case and core of the battery.
- Unlike [7], which relies on a thermal–electrochemical model for LiBs, this study examines temperature variations in each internal component of ASSBs. This includes the case surface temperature near the cathode, cathode, electrolyte, anode, and the case surface temperature near the anode.
- This article has a solid validation process using ANSYS Transient Thermal Analysis to confirm the accuracy and reliability of the presented thermal model.
- This study utilizes an electrochemical model for temperature estimation in ASSBs. Moreover, it pioneers the estimation of temperature variations in various components within ASSBs. In contrast, existing studies such as [8] and [9] focus on the liquid electrolyte and use the Equivalent Circuit Model.
- Unlike [10], which uses the 3rd order of the Padé approximation, this article employs the 5th order of the Padé approximation. This choice is made due to the higher accuracy achieved by the 5th order compared to the 3rd order, as evidenced by numerical simulations.

The remainder of this article is organized as follows: Section II introduces the thermal model. Section III delves into the electrochemical model and its reduction using a fifth-order Padé approximation. Model verification is discussed in Section IV. Section V covers optimal sensor placement and the Kalman filter algorithm employed for temperature estimation. The simulation results are presented in Section VI. Finally, Section VII outlines conclusions and discusses future work.

II. Thermal Model

In Figure 1(a), a schematic of an ASSB is shown. The outer black line marks the system's boundaries, simulating a thermal chamber for the experimental study of the ASSB.

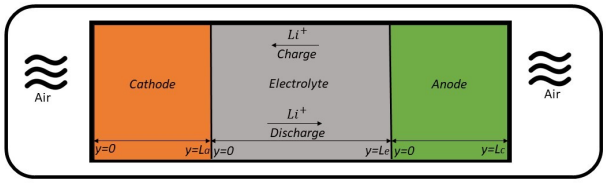

(a) ASSB schematic.

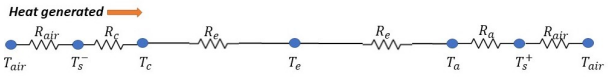

(b) Thermal model.

Fig. 1: ASSB model.

In Figure 1(b), the diagram shows the heat exchange within the battery using thermal resistances. Heat is generated at the cathode due to electrochemical reactions. Here, T_{air} and R_{air} denote air temperature and resistance. $T_{\text{s}-}$ is

P. Ferreira and S.-X. Tang (corresponding author) are with the Department of Mechanical Engineering, Texas Tech University, Lubbock, USA. patferre@ttu.edu, shuxia.tang@ttu.edu.

the case surface temperature near the cathode, and R_{c} is the cathode's thermal resistance. T_{c} represents the cathode temperature, while R_{e} is the electrolyte's thermal resistance. T_{e} is the electrolyte temperature. R_{a} and T_{a} relate to the anode, with T_{s^+} being the case surface temperature near the anode.

Assumption 1. *Within the system where the ASSB was considered, the adiabatic condition prevails, indicating no heat exchange between the system and its surroundings. This condition implies a uniform temperature distribution within the system, resulting in an equilibrium state where there is no net transfer of energy into or out of the system. Mathematically, this equilibrium is expressed as:*

$$\dot{T}_i(t) = \frac{Q_i(t)}{\rho_i c_{p,i}}, \tag{II.1}$$

where $\dot{T}_i$ represents the rate of increase in temperature over time, ρ_i denotes the density of the material in the system, $c_{p,i}$ stands for the heat capacity of the material within the system, and Q_i represents the heat generated within the ASSBs, for $i \in \{s^-,\, c,\, e,\, a,\, s^+\}$.

The heat generation, $Q_i(t)$, is normalized by dividing it by the volume, v_i, resulting in the unit of measurement W/m^3. This heat generation, $Q_i(t)$, in an ASSBs is depicted in (II.2), as follows:

$$Q_i(t) = \frac{S(t) + q_{\mathrm{cond},i}(t)}{v_i}, \tag{II.2}$$

where $S(t)$ represents the heat generated within batteries as a result of chemical reactions occurring inside the battery, and $q_{\mathrm{cond},i}(t)$ denotes the portion of heat generated caused by interactions between the ASSBs components, and v_i is the volume of each part of the ASSBs, for $i \in \{\mathrm{s}^-,\, \mathrm{c},\, \mathrm{e},\, \mathrm{a},\, \mathrm{s}^+\}$.

Since $S(t)$ is produced as a function of chemical reactions, it will be discussed in Section III where the electrochemical model is explained.

Using Figure 1(b) as a guide, the conduction heat in each part of the ASSB is determined. Following the Heat generation direction, the first heat conduction is between the outside air and the case surface near to cathode (left boundary of the cathode):

$$q_{\mathrm{cond,s}^-}(t) = \frac{T_{\mathrm{air}}(t) - T_{\mathrm{s}^-}(t)}{R_{\mathrm{air}}}. \tag{II.3}$$

The next is the heat conduction between the case surface near to cathode (left boundary of the cathode) and the cathode, given by:

$$q_{\mathrm{cond,c}}(t) = \frac{T_{\mathrm{s}^-}(t) - T_{\mathrm{c}}(t)}{R_{\mathrm{c}}}. \tag{II.4}$$

Following that is the heat conduction between the cathode and electrolyte:

$$q_{\mathrm{cond,e}}(t) = \frac{T_{\mathrm{c}}(t) - T_{\mathrm{e}}(t)}{R_{\mathrm{e}}}. \tag{II.5}$$

Then the heat conduction between the electrolyte and anode:

$$q_{\mathrm{cond,a}}(t) = \frac{T_{\mathrm{e}}(t) - T_{\mathrm{a}}(t)}{R_{\mathrm{e}}}. \tag{II.6}$$

Between the anode and the the case surface temperature near to the anode (right boundary of the anode):

$$q_{\mathrm{cond,s}^+}(t) = \frac{T_{\mathrm{a}}(t) - T_{\mathrm{s}^+}(t)}{R_{\mathrm{a}}}. \tag{II.7}$$

Finally, between the outside air and the case surface temperature near to the anode (right boundary of the anode):

$$q_{\mathrm{cond,air}}(t) = \frac{T_{s^+}(t) - T_{\mathrm{air}}(t)}{R_{\mathrm{air}}}. \tag{II.8}$$

A. Temperature Model for Each Component of the Battery

In this article, the cathode, electrolyte, and anode of the ASSB are stacked. This stacking configuration simplifies the analysis, resulting in a "quintuple" model consisting of five ODEs. These ODEs cover the case surface near to cathode (left boundary of the cathode), the cathode itself, the electrolyte, the anode, and the case surface temperature near to the anode (right boundary of the anode). This modeling approach is applicable for addressing temperature-related issues in pouch, prismatic, and coin ASSB cells. By applying Equation (II.1) in each part of the ASSB, the following temperatures are determined:

1) The temperature of the left boundary of the cathode, $T_{s^-}(t)$: Applying Equations (II.3) and (II.4), the minus sign indicates heat extraction from the battery during the interaction between the cathode and the surface.

$$\dot{T}_{s^-}(t) = \frac{T_{\mathrm{air}}(t) - T_{\mathrm{s}^-}(t)}{\lambda_{\mathrm{air}} R_{\mathrm{air}}} - \frac{T_{\mathrm{s}^-}(t) - T_{\mathrm{c}}(t)}{\lambda_{\mathrm{air}} R_{\mathrm{c}}},$$

where $\lambda_{\mathrm{air}} = v_{\mathrm{air}} \rho_{\mathrm{air}} c_{p_{\mathrm{air}}}$, with v_{air} as the volume of the air in contact with the battery, ρ_{air} as the density of air, and $c_{p_{\mathrm{air}}}$ as the heat capacity of air.

2) Cathode Temperature $T_c(t)$: In the cathode, heat is generated through electrochemical reactions. Applying Equation (II.4) to account for heat conduction, the cathode temperature is determined as follows:

$$\dot{T}_{\mathrm{c}}(t) = \frac{T_{\mathrm{s}^-}(t) - T_{\mathrm{c}}(t)}{\lambda_{\mathrm{c}} R_{\mathrm{c}}} + \frac{S(t)}{\lambda_{\mathrm{c}}},$$

where $\lambda_{\mathrm{c}} = v_{\mathrm{c}} \rho_{\mathrm{c}} c_{p_{\mathrm{c}}}$, with v_{c} as the volume of the cathode, ρ_{c} as the density of the cathode, and $c_{p_{\mathrm{c}}}$ as the heat capacity of the cathode.

3) Electrolyte Temperature $T_e(t)$: Similar to the cathode temperature, the electrolyte temperature is defined using the heat conduction equation (II.5) as follows:

$$\dot{T}_{\mathrm{e}}(t) = \frac{T_{\mathrm{c}}(t) - T_{\mathrm{e}}(t)}{\lambda_{\mathrm{e}} R_{\mathrm{e}}} + \frac{S(t)}{\lambda_{\mathrm{e}}},$$

where $\lambda_{\mathrm{e}} = v_{\mathrm{e}} \rho_{\mathrm{e}} c_{p_{\mathrm{e}}}$, with v_{e} as the volume of the electrolyte, ρ_{e} as the density of the electrolyte, and $c_{p_{\mathrm{e}}}$ as the heat capacity of the electrolyte.

4) Anode Temperature $T_a(t)$: Similar to the cathode and electrolyte temperatures, and considering the heat conduction Equation (II.6), the anode temperature is given by:

$$\dot{T}_a(t) = \frac{T_e(t) - T_a(t)}{\lambda_{\mathrm{a}} R_e} + \frac{S(t)}{\lambda_{\mathrm{a}}},$$

where $\lambda_{\mathrm{a}} = v_{\mathrm{a}} \rho_{\mathrm{a}} c_{p_{\mathrm{a}}}$, with v_{a} as the volume of the anode, ρ_{a} as the density of the anode, and $c_{p_{\mathrm{a}}}$ as the heat capacity of the anode.

5) The temperature of the right boundary of the anode, $T_{s^+}(t)$: Similar to $T_{\mathrm{s}^-}(t)$, and utilizing Equations (II.7) and (II.8), $T_{\mathrm{s}^+}(t)$ is obtained. The plus sign indicates that the anode deposits heat into the surface.

$$\dot{T}_{\mathrm{s}^+}(t) = \frac{T_{\mathrm{s}^+}(t) - T_{\mathrm{air}}(t)}{\lambda_{\mathrm{air}} R_{\mathrm{air}}} + \frac{T_{\mathrm{a}}(t) - T_{\mathrm{s}^+}(t)}{\lambda_{\mathrm{air}} R_{\mathrm{a}}}.$$

B. Quintuple state-space system

The quintuple state-space representation of the system is:

$$\begin{aligned} \dot{\boldsymbol{T}}(t) &= \mathcal{A}\boldsymbol{T}(t) + \mathcal{B}\boldsymbol{u}(t) + \boldsymbol{w}(t), \\ y(t) &= \mathcal{C}\boldsymbol{T}(t) + v(t), \\ \boldsymbol{w} &\sim (0, Q), \\ v &\sim (0, R), \end{aligned}$$

where

$$\mathcal{A} = \begin{bmatrix} \frac{-R_{\mathrm{c}} - R_{\mathrm{air}}}{\lambda_{\mathrm{air}} R_{\mathrm{c}} R_{\mathrm{air}}} & \frac{1}{\lambda_{\mathrm{air}} R_{\mathrm{c}}} & 0 & 0 & 0 \\ \frac{1}{\lambda_{\mathrm{c}} R_{\mathrm{c}}} & \frac{-1}{\lambda_{\mathrm{c}} R_{\mathrm{c}}} & 0 & 0 & 0 \\ 0 & \frac{1}{\lambda_{\mathrm{e}} R_{\mathrm{e}}} & \frac{-1}{\lambda_{\mathrm{e}} R_{\mathrm{e}}} & 0 & 0 \\ 0 & 0 & \frac{1}{\lambda_{\mathrm{a}} R_{\mathrm{e}}} & \frac{-1}{\lambda_{\mathrm{a}} R_{\mathrm{e}}} & 0 \\ 0 & 0 & 0 & \frac{1}{\lambda_{\mathrm{air}} R_{\mathrm{a}}} & \frac{R_{\mathrm{a}} - R_{\mathrm{air}}}{\lambda_{\mathrm{air}} R_{\mathrm{a}} R_{\mathrm{air}}} \end{bmatrix},$$

$$\mathbf{T}(t) = \begin{bmatrix} T_s^-(t) & T_c(t) & T_e(t) & T_a(t) & T_s^+(t) \end{bmatrix}^{\mathrm{tr}},$$

$$\mathcal{B} = \begin{bmatrix} \frac{1}{\lambda_{\mathrm{air}} R_{\mathrm{air}}} & 0 & 0 & 0 & \frac{-1}{\lambda_{\mathrm{air}} R_{\mathrm{air}}} \\ 0 & \frac{1}{\lambda_{\mathrm{c}}} & \frac{1}{\lambda_{\mathrm{e}}} & \frac{1}{\lambda_{\mathrm{a}}} & 0 \end{bmatrix}^{\mathrm{tr}}$$

$$\mathbf{u}(t) = \begin{bmatrix} T_{\mathrm{air}}(t) & S(t) \end{bmatrix}^{\mathrm{tr}}.$$

Here, $\mathbf{T}(t)$ represents the state vector of the system's temperature, $\mathbf{u}(t)$ denotes the inputs of the thermal model, and $S(t)$ represents the heat generated by electrochemical reactions, the derivation of which will be presented in Section (III) using the electrochemical model. $\boldsymbol{w}(t)$ and $v(t)$ are considered independent, zero-mean, white noise with covariances Q and R, respectively. $\mathcal{C}$ will be discussed in Section V.

III. Heat Generated S derived from Electrochemical model

The components of a typical ASSB are represented in Figure 1(a). The anode is made of metallic lithium, the traditional $LiCoO_2$ provides the foundation of the Cathode, and an amorphous Li_3PO_4 is the electrolyte that separates the anode from cathode [11]. The operating principle of the ASSB consists of lithium metal at the anode is oxidized during discharge, producing Li^+ and an electron. The former flows via the solid electrolyte, while the latter travels through the external circuit to the cathode, where the cathode active material forms an intercalated compound. Li^+ migrate back to the anode and are stored as metallic lithium intercalated between graphene layers during charging because the flow of Li^+ and electrons is reversed during this process [12].

A. PDE Model for Concentration

The substantial exchange current density for the metallic lithium makes the anode's charge transfer overpotential of anode sufficiently minimal, therefore the anode's charge transfer kinetics are neglected [13].

The concentration of Li^+ is regulated by Fick's second law, as described in [10], as follows:

$$\frac{\partial c_{\mathrm{s}}^-}{\partial t}(y,t) = D_{\mathrm{s}}^- \frac{\partial^2 c_{\mathrm{s}}^-}{\partial y^2}(y,t), \tag{III.1}$$

$$D_{\mathrm{s}}^- \frac{\partial c_{\mathrm{s}}^-(L_p,t)}{\partial y} = \frac{I(t)}{FA}, \tag{III.2}$$

$$D_{\mathrm{s}}^- \frac{\partial c_{\mathrm{s}}^-(0,t)}{\partial y} = 0, \tag{III.3}$$

$$c_{\mathrm{s}}^-(y,0) = c_{\mathrm{s}^-,0}, \tag{III.4}$$

where c_{s}^- is the concentration of Li^+ in the cathode, D_{s}^- is the diffusion coefficient, F is Faraday's constant, A is the surface area, and $I(t)$ is the current [14].

The main ionic transport mechanisms in the Li_3PO_4 solid electrolyte are diffusion and migration of Li^+. This process is described by [10]:

$$\frac{\partial c_{\mathrm{e}}}{\partial t}(y,t) = \frac{2 D_{\mathrm{Li}^+} D_{\mathrm{n}^-}}{D_{\mathrm{Li}^+} + D_{\mathrm{n}^-}} \frac{\partial^2 c_{\mathrm{e}}}{\partial y^2}(y,t) + \mathrm{r}(c_{\mathrm{e}}(y,t)), \tag{III.5}$$

$$\frac{\partial c_{\mathrm{e}}(0,t)}{\partial y} = -\frac{I(t)}{2FAD_{\mathrm{Li}^+}}, \tag{III.6}$$

$$\frac{\partial c_{\mathrm{e}}(L,t)}{\partial y} = -\frac{I(t)}{2FAD_{\mathrm{Li}^+}}, \tag{III.7}$$

$$c_{\mathrm{e}}(y,0) = \delta c_{\mathrm{e},0}, \tag{III.8}$$

where c_{e} is the concentration in the electrolyte, D_{Li^+} and D_{n^-} are diffusion coefficients of Li^+ and n^- in the solid electrolyte, δ is the fraction of free Li^+ in equilibrium, and r represents the net charge carrier generation:

$$\mathrm{r}(c_{\mathrm{e}}(y,t)) = \frac{\delta^2 k_r c_{\mathrm{e},0} \left(c_{\mathrm{e},0} - c_{\mathrm{e}}\right)}{1-\delta} - k_r c_{\mathrm{e}}(y,t)^2, \tag{III.9}$$

where k_r is the Li^+ generation reaction rate constant.

B. Reduced-Order Model for Concentration

To mitigate operational costs associated with resolving PDEs, the Padé approximation method is employed to derive a linearized representation of the model. The Wolfram Alpha platform was utilized for the Padé approximation calculation using the code: *pade*.

The process begins with transforming the PDE into the Laplace domain, which enables its representation with exponential terms. Subsequently, these terms are translated into ODEs. Finally, Padé approximation is employed to approximate the solution, ensuring computational efficiency and accuracy. The Padé approximation for the cathode and solid electrolyte will be discussed sequentially.

$$\frac{C_{\rm s}^{-}(0,s)}{\mathrm{I}(s)} = \frac{\frac{1029037L_p^7s^4}{346781323848960AD_{\rm s}^{-4}F} - \frac{560401L_p^5s^3}{562956694560AD_{\rm s}^{-3}F} + \frac{1281433L_p^3s^2}{7217393520AD_{\rm s}^{-2}F} - \frac{2290747L_ps}{120289892AD_{\rm s}^{-}F} + \frac{1}{AFL_p}}{\frac{4585922449L_p^8s^5}{15605159573203200D_{\rm s}^{-4}} + \frac{269197963L_p^6s^4}{3940696861920D_{\rm s}^{-3}} + \frac{38518909L_p^4s^3}{7217393520D_{\rm s}^{-2}} + \frac{53272705L_p^2s^2}{360869676D_{\rm s}^{-}} + s} \tag{III.10}$$

$$\frac{C_{\rm s}^{-}(L_p,s)}{\mathrm{I}(s)} = \frac{\frac{L_p^7s^4}{765765AD_{\rm s}^{-4}F} + \frac{4L_p^5s^3}{9945AD_{\rm s}^{-3}F} + \frac{7L_p^3s^2}{255AD_{\rm s}^{-2}F} + \frac{8L_ps}{17AD_{\rm s}^{-}F} + \frac{1}{AFL_p}}{\frac{L_p^8s^5}{34459425D_{\rm s}^{-4}} + \frac{2L_p^6s^4}{69615D_{\rm s}^{-3}} + \frac{L_p^4s^3}{255D_{\rm s}^{-2}} + \frac{7L_p^2s^2}{51D_{\rm s}^{-}} + s}, \tag{III.11}$$

$$\frac{C_{\rm e}(0,s)}{\mathrm{I}(s)} = \frac{\frac{L_e^9s^4}{12189864960AD_e^{+4}D_{Li^+}F} + \frac{L_e^7s^3}{6511680AD_e^{+3}D_{Li^+}F} + \frac{7L_e^5s^2}{103360AD_e^{+2}D_{Li^+}F} + \frac{L_e^3s}{114AD_e^{+}D_{Li^+}F} + \frac{L_e}{4AD_{Li^+}F}}{\frac{L_e^{10}s^5}{670442572800D_e^{+5}} + \frac{L_e^8s^4}{112869120D_e^{+4}} + \frac{7L_e^6s^3}{930240D_e^{+3}} + \frac{7L_e^4s^2}{3876D_e^{+2}} + \frac{9L_e^2s}{76D_e^{+}} + 1}, \tag{III.12}$$

1) Padé Approximation for Cathode Concentration: The transcendental transfer functions of cathode is:

$$\frac{C_{\rm s}^{-}(0,s)}{\mathrm{I}(s)} = \frac{2\exp\left(L_{\rm p}s^*\right)}{FAs^*D_{\rm s}^{-}\left(-1+\exp\left(2L_{\rm p}s^*\right)\right)}, \tag{III.13}$$

$$\frac{C_{\rm s}^{-}(L_{\rm p},s)}{\mathrm{I}(s)} = \frac{1+\exp\left(2L_{\rm p}s^*\right)}{FAs^*D_{\rm s}^{-}\left(-1+\exp\left(2L_{\rm p}s^*\right)\right)}, \tag{III.14}$$

where $s^* \triangleq \sqrt{\frac{s}{D_{\rm s}^{-}}}$. Note that the terms $\sqrt{D_{\rm s}^{-}}$ in the denominators of both trasncendel transfer function in [10] are replaced by $D_{\rm s}^{-}$ here.

Both transcendental transfer functions are transformed into low-order and fractional transfer functions using the Padé approximation approach. Equations (III.10) and (III.11) present the fifth-order Padé approximation for the concentration of Li^+ at the cathode when $y = 0$ and when $y = L_p$.

2) Padé Approximation for Electrolyte Concentration: The diffusion dynamics in the electrolyte change from linear to quadratic because of the r term in (III.5), which is a function of the Li^+ concentration [10]. To construct a linear PDE and deduce an analytical solution for (III.5), the r component is neglected due to its small contribution. The transcendental transfer function for electrolyte is given by [10]:

$$\frac{C_{\rm e}(0,s)}{I(s)} = -\frac{C_{\rm e}(L_{\rm e},s)}{I(s)} = \frac{-1+\exp\left(L_{\rm e}{s_{\rm e}}^*\right)}{2FA{s_{\rm e}}^*D_{\rm e}^{+}\left(1+\exp\left(L_{\rm e}{s_{\rm e}}^*\right)\right)}, \tag{III.15}$$

where ${s_{\rm e}}^* \triangleq \sqrt{\frac{s}{D_{\rm e}^{+}}}$.

The fifth-order Padé approximation for the Li^+ concentration in the electrolyte, denoted as (III.12), is defined where $D_{\rm e}^{+}$ is given as $\frac{2D_{\rm e}D_{\rm e}^{-}}{D_{\rm e}+D_{\rm e}^{-}}$.

C. Heat Generated $S(t)$

The charge transfer overpotential, the mass transfer overpotential caused by the flow of Li^+ in the solid-state electrolyte, and the diffusion overpotential in the interface of the intercalation electrode combine to form the battery's total overpotential, which is denoted by [10]:

$$\eta_{\rm t}(t) = \eta_{\rm ct}(t) + \eta_{\rm mt}(t) + \eta_{\rm d}(t).$$

A simplified version of $\eta_{\rm ct}$ is given by [11]:

$$\eta_{\rm ct}(t) = \frac{2RT}{F}\sinh\left(\frac{-I(t)}{2i_{0,\rm pos}(t)}\right),$$

where

$$i_{0,\rm pos}(t) = FAk_{\rm pos}\left(\frac{(c_{\max}-c_{\rm s}^{-})c_{\rm e}}{(c_{\max}-c_{\min})c_{\rm e,0}}\right)^{\alpha_{\rm pos}} \times \left(\frac{(c_{\rm s}^{-}-c_{\min})}{(c_{\max}-c_{\min})}\right)^{1-\alpha_{\rm pos}}.$$

The mass-transfer overpotential $\eta_{\rm mt}$ and the diffusion overpotential $\eta_{\rm d}$ are given by [11], as follows:

$$\eta_{\rm mt}(t) = \frac{L_eRTI(t)}{c_{\rm Li}^{+}F^2A(D_{\rm Li}^{+}+D_{\rm n}^{-})},$$

$$\eta_{\rm d}(t) = E_{\rm eq}(\theta_s(t)) - E_{\rm eq}(\bar{\theta_s}(t)).$$

Here, $E_{\rm eq}$ represents the equilibrium potential, as discussed in [10]. The parameters $\theta_s(t)$, $\bar{\theta}_s(t)$, and $C_{\rm Lis,avg}$ are used to determine the value of $E_{\rm eq}$, as follows:

$$\theta_s(t) = \frac{C_{\rm Lis}(L_p,t)}{C_{\rm Lis,max}},$$

$$\bar{\theta}_s(t) = \frac{C_{\rm Lis,avg}}{C_{\rm Lis,max}},$$

$$C_{\rm Lis,avg}(L_p,t) = \frac{IL_p}{6FAD_{\rm Lis}} + C_{\rm Lis}(0,t).$$

The terminal voltage is given by [11]:

$$V(t) = E_{\rm eq}(\bar{\theta_s}(t)) + \eta_{\rm t}(t).$$

The result of multiplying current and voltage informs us about the number of electrons moving through a system, along with the energy each electron expends as heat, ultimately providing the total heat production [15, Chapter 1, Section 1.4.1].

$$S(t) = V(t)I(t). \tag{III.16}$$

IV. Thermal model verification

A 2D model was developed in ANSYS using the transient thermal analysis, which was then compared with a thermal model implemented in Matlab. The electrochemical model, represented by Equation (III.16), was used to calculate internal heat generation in the anode, electrolyte, and cathode.

In the ANSYS simulation, a transient 2D PDE was solved with a spatial step size of 0.105×10^{-9} meters in both dimensions. In contrast, Matlab utilized ODEs, focusing solely on temporal dynamics without considering spatial

increments. Both simulations shared a temporal step size of $\Delta t = 1$ second and concluded at a final simulation time of 1790 seconds.

Figure 2 compares ANSYS transient thermal analysis with Matlab, showing minimal temperature discrepancies. Notably, at 1000 seconds, the temperatures reach equilibrium where the local errors between temperatures are very low: 0.076°C for the cathode, 1.09°C for the electrolyte, and 0.033°C for the anode. This demonstrates the accuracy of the presented thermal model.

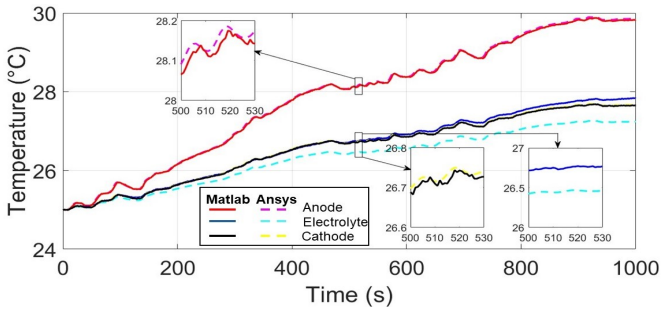

Fig. 2: Thermal model comparision with ANSYS Transient Thermal Analysis.

V. Optimal Sensor Placement and Kalman Filter

A sensor placement study was conducted to determine the most realistic sensor placement. When considering only one sensor, there is only one observable option. In this particular configuration, the sensor is placed at the right boundary of the anode, as shown in Figure 1(a). Below, the value of $\mathcal{C}$ for this specific placement is given by:

$$\mathcal{C} = \begin{bmatrix} 0 & 0 & 0 & 0 & 1 \end{bmatrix}.$$

With the sensor placement established, the application of the Kalman filter was motivated by its effectiveness in accurately estimating temperature states, especially when simulating sensors with Gaussian noise in the battery. The state estimation update is given by: $\dot{\hat{\mathbf{T}}} = \mathcal{A}\hat{\mathbf{T}} + \mathcal{B}\mathbf{u} + K(y - \mathcal{C}\hat{\mathbf{T}})$, where $K = P\mathcal{C}^{\mathrm{tr}}R^{-1}$ and $\dot{P} = -P\mathcal{C}^{\mathrm{T}}R^{-1}\mathcal{C}P + \mathcal{A}P + P\mathcal{A}^{\mathrm{tr}} + Q$.

VI. Simulation Results

The simulation was performed using MATLAB on a personal computer from SAMSUMG equipped with an Intel i5-10210U 1.6 GHz CPU and 31.8 GB of RAM.

The thermal resistances between the internal components are determined using the formula $R_i = \frac{L_i}{k_i A_i}$, where L_i represents the length, k_i represents the thermal conductivity, and A_i represents the area, for $i \in \{\mathrm{s}^-, \mathrm{c}, \mathrm{e}, \mathrm{a}, \mathrm{s}^+, \mathrm{air}\}$.

The Equilibrium potential E_{eq} in the $LiCoO_2$ cathode is calculated as [10]:

$$E_{eq}(\theta_s(t)) = \frac{\begin{array}{r}(-219.027 + 322.003\theta_s^2 - 198.242\theta_s^4 \\ - 44.337 + 36.643\theta_s^2 + 3.430\theta_s^4)\end{array}}{\begin{array}{r}(354.911\theta_s^6 - 467.807\theta_s^8 + 207.168\theta_s^{10} \\ 113.081\theta_s^6 - 182.567\theta_s^8 + 80.3097\theta_s^{10})\end{array}}.$$

The electrochemical parameters used in the simulation were: $A = 0.0001\,\mathrm{m}^2$, $C_{\max} = 2.33 \times 10^4\,\mathrm{mol\ m}^{-3}$, $C_{e,0} = 6.01 \times 10^4\,\mathrm{mol\ m}^{-3}$, $D_{Li}^{+} = 0.9 \times 10^{-15}\,\mathrm{m^2 s^{-1}}$, $D_s^{-} = 1.76 \times 10^{-15}\,\mathrm{m^2 s^{-1}}$, $D_n^{-} = 5.1 \times 10^{-15}\,\mathrm{m^2 s^{-1}}$, $F = 96485.3365\,\mathrm{C\ mol}^{-1}$, $L_e = 1500 \times 10^{-9}\,\mathrm{m}$, $L_p = 320 \times 10^{-9}\,\mathrm{m}$, $\alpha_{\mathrm{pos}} = 0.6$ [14]. Additionally, $C_{\min} = 1.1645 \times 10^4\,\mathrm{mol\ m}^{-3}$, $k_n = 1 \times 10^{-2}\,\mathrm{m^3 mol^{-1} s^{-1}}$, $k_p = 5.1 \times 10^{-4}\,\mathrm{m^3 mol^{-1} s^{-1}}$ [10].

The thermal parameters are: $\rho_{\mathrm{a}} = 534\,\mathrm{kg\ m}^{-3}$ [16], $\rho_{\mathrm{e}} = 710\,\mathrm{kg\ m}^{-3}$, $c_{pe} = 1252\,\mathrm{J\ kg^{-1} K^{-1}}$ [17], $\rho_{\mathrm{c}} = 4790\,\mathrm{kg\ m}^{-3}$ [18], $k_a = 85\,\mathrm{W\ m^{-1} K^{-1}}$ [19], $k_e = 0.7\,\mathrm{W\ m^{-1} K^{-1}}$ [20], $k_c = 3.7\,\mathrm{W\ m^{-1} K^{-1}}$ [21], $c_{pa} = 3600\,\mathrm{J\ kg^{-1} K^{-1}}$ [22], $c_{pc} = 730\,\mathrm{J\ kg^{-1} K^{-1}}$ [23].

The battery simulation was conducted with a set capacity of 100mAh. The initial temperatures of the battery, both internal and external, were set to 25°C to simulate a resting start. In the Kalman filter, the process noise covariance matrix Q was chosen as $2 \times \mathrm{I}_5$, the measurement noise covariance R was chosen as 0.025, the error covariance P was chosen as 1, and the initial condition was set to 20°C. The simulation used the Urban Dynamometer Driving Schedule (UDDS) as input, as depicted in Figure 3.

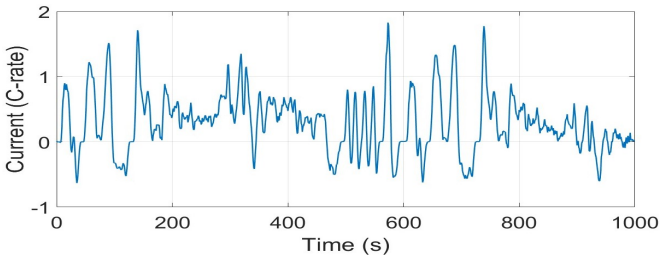

Fig. 3: Current profile.

Figure 4 shows the temperatures of the battery components. Inside the battery the anode temperature T_a is the highest due to the exothermic nature of lithium-ion reactions, where lithium-ions move from the anode to the cathode, resulting in the release of energy in the form of heat. This exothermic reaction at the anode significantly contributes to the elevated anode temperature.

In contrast, the cathode temperature T_c is lower than the anode temperature. This lower cathode temperature results from the relatively lower heat generation associated with cathode electrochemical processes, where materials such as $LiCoO_2$ undergo less exothermic reactions compared to the anode.

The solid electrolyte temperature T_e is observed to be higher than the cathode temperature but lower than the anode temperature. This temperature ranking in the solid electrolyte Li_3PO_4 is influenced by the heat transfer dynamics and thermal properties of the material. Positioned between the lithium anode and the cathode containing $LiCoO_2$, the solid electrolyte experiences heat transfer from both sides. The anode, being the primary source of heat due to exothermic reactions, elevates the temperature of the electrolyte, while the cathode contributes less heat. This differential heat contribution results in the observed temperature ranking, with

the solid electrolyte maintaining an intermediate temperature level within the battery structure.

The surface temperature T_s^+ is slightly higher than the anode temperature, as expected due to direct heat transfer from the anode to the surface and the battery. Conversely, the surface temperature T_s^- is the lowest, which aligns with its direct contact with the cathode, as anticipated.

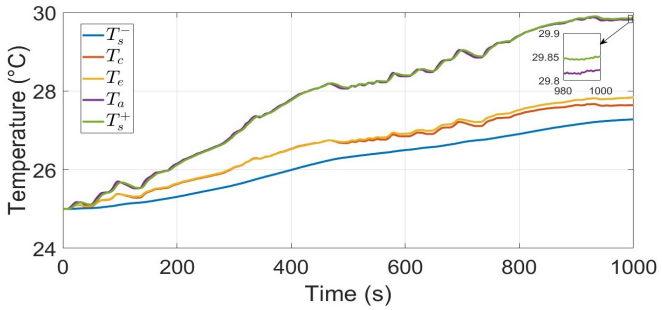

Fig. 4: Temperature states in ASSB.

In Figure 5, the results of applying the Kalman filter with optimal sensor placement are shown.

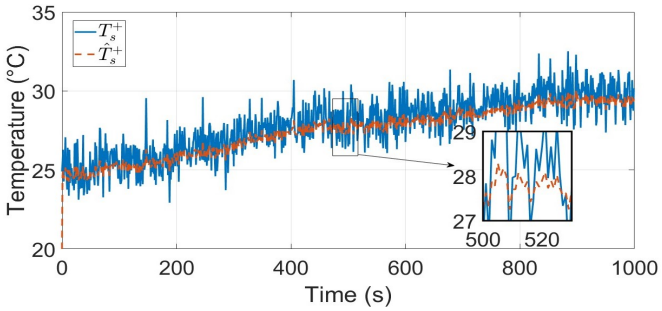

Fig. 5: Comparison between the true output and the output estimated by the Kalman filter.

VII. Conclusion and Future Work

This article presents a model for efficient ASSB temperature estimation using an electrochemical model for heat generation. Verification with ANSYS showed minimal local errors. Simulations indicate that the anode reaches the highest temperature due to exothermic reactions, and the Kalman filter estimates are very close to the true model.

Future work will focus on simultaneous temperature and State-of-Charge estimation under non-adiabatic conditions, with adaptive observers being developed to address model uncertainties.

References

[1] Takeshi Uyama, Takao Inoue, and Kazuhiko Mukai. Realizing the ultimate thermal stability of a lithium-ion battery using two zero-strain insertion materials. *ACS Applied Energy Materials*, 1(10):5712–5717, 2018.

[2] Yuki Kato, Satoshi Hori, Toshiya Saito, Kota Suzuki, Masaaki Hirayama, Akio Mitsui, Masao Yonemura, Hideki Iba, and Ryoji Kanno. High-power all-solid-state batteries using sulfide superionic conductors. *Nature Energy*, 1(4):1–7, 2016.

[3] Yonglin Huang, Bowen Shao, and Fudong Han. Solid-state batteries: An introduction. In *Solid State Batteries Volume 1: Emerging Materials and Applications*, pages 1–20. ACS Publications, 2022.

[4] Rusong Chen, Qinghao Li, Xiqian Yu, Liquan Chen, and Hong Li. Approaching practically accessible solid-state batteries: stability issues related to solid electrolytes and interfaces. *Chemical reviews*, 120(14):6820–6877, 2019.

[5] Arumugam Manthiram. A reflection on lithium-ion battery cathode chemistry. *Nature communications*, 11(1):1550, 2020.

[6] Chanwoo Park and Arun K Jaura. Dynamic thermal model of li-ion battery for predictive behavior in hybrid and fuel cell vehicles. Technical report, SAE Technical Paper, 2003.

[7] Shu-Xia Tang, Leobardo Camacho-Solorio, Yebin Wang, and Miroslav Krstic. State-of-charge estimation from a thermal–electrochemical model of lithium-ion batteries. *Automatica*, 83:206–219, 2017.

[8] Ting Cai, Anna G Stefanopoulou, and Jason B Siegel. Modeling li-ion battery temperature and expansion force during the early stages of thermal runaway triggered by internal shorts. *Journal of The Electrochemical Society*, 166(12):A2431, 2019.

[9] Xinfan Lin, Anna G Stefanopoulou, Hector E Perez, Jason B Siegel, Yonghua Li, and R Dyche Anderson. Quadruple adaptive observer of the core temperature in cylindrical li-ion batteries and their health monitoring. In *2012 American Control Conference (ACC)*, pages 578–583. IEEE, 2012.

[10] Zhongwei Deng, Xiaosong Hu, Xianke Lin, Le Xu, Jiacheng Li, and Wenchao Guo. A reduced-order electrochemical model for all-solid-state batteries. *IEEE Transactions on Transportation Electrification*, 7(2):464–473, 2020.

[11] Kushagra Upreti, Isaiah Oyewole, Xianke Lin, and Youngki Kim. On simplification of a solid-state battery model for state estimation. In *2019 IEEE Conference on Control Technology and Applications (CCTA)*, pages 487–492. IEEE, 2019.

[12] Artur M Suzanowicz, Cindy W Mei, and Braja K Mandal. Approaches to combat the polysulfide shuttle phenomenon in li–s battery technology. *Batteries*, 8(5):45, 2022.

[13] Dong Zhang, Shu-Xia Tang, Luis D. Couto, and Venkatasubramanian Viswanathan. PDE observer for all-solid-state batteries via an electrochemical model. In *2021 IEEE Conference on Control Technology and Applications (CCTA)*, pages 51–56, 2021.

[14] D Danilov, RAH Niessen, and PHL Notten. Modeling all-solid-state li-ion batteries. *Journal of the Electrochemical Society*, 158(3):A215, 2010.

[15] Alexandra Von Meier. *Electric power systems: a conceptual introduction*. John Wiley & Sons, 2006.

[16] Mihir Parekh and Christopher Rahn. Dendrite suppression and energy density in metal batteries with electrolyte flow through perforated electrodes. In *ASME International Mechanical Engineering Congress and Exposition*, volume 84560, page V008T08A018. American Society of Mechanical Engineers, 2020.

[17] Chemister database. [Online] http://chemister.ru/Database/properties-en.php?dbid=1id=5621.

[18] Eric Jianfeng Cheng, Nathan John Taylor, Jeff Wolfenstine, and Jeff Sakamoto. Elastic properties of lithium cobalt oxide (licoo2). *Journal of Asian Ceramic Societies*, 5(2):113–117, 2017.

[19] Shane Park, Sang-Hoon Jung, Chi-Young Han, Soon-Young Kim, Jong-Kyung Kim, Gyoo-Dong Jeun, Min-Goo Hur, and Jong-Seo Chai. A study on thermal optimization of lithium target design for accelerator-based bnct. In *Proceedings of the Korean Nuclear Society Conference*, pages 883–884. Korean Nuclear Society, 2005.

[20] Cheng-Wei Wu, Xue Ren, Wu-Xing Zhou, Guofeng Xie, and Gang Zhang. Thermal stability and thermal conductivity of solid electrolytes. *APL Materials*, 10(4), 2022.

[21] Jiung Cho, Mark D Losego, Hui Gang Zhang, Honggyu Kim, Jianmin Zuo, Ivan Petrov, David G Cahill, and Paul V Braun. Electrochemically tunable thermal conductivity of lithium cobalt oxide. *Nature Publishing Group UK London*, 2014.

[22] MMTA Minor Metals Trade Association. [Online] https://mmta.co.uk/metals/li.

[23] Petronela Gotcu-Freis, Damian M Cupid, Magnus Rohde, and Hans J Seifert. New experimental heat capacity and enthalpy of formation of lithium cobalt oxide. *The Journal of Chemical Thermodynamics*, 84:118–127, 2015.